

# Formation of $\text{CaCO}_3$ Deposits on Hard Surfaces—Effect of Bulk Solution Conditions and Surface Properties

Hao Wang,<sup>†,‡</sup> Viveka Alfredsson,<sup>†</sup> Juergen Tropsch,<sup>§</sup> Roland Ettl,<sup>§</sup> and Tommy Nylander\*,<sup>†</sup>

<sup>†</sup>Physical Chemistry, Lund University, P.O. Box 124, SE-221 00 Lund, Sweden

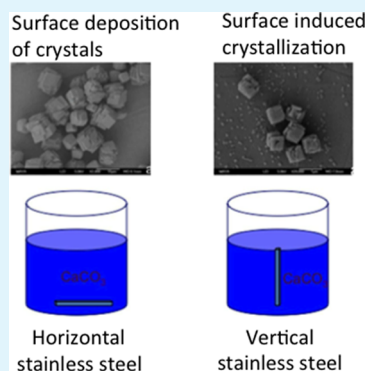
<sup>‡</sup>State Key Laboratory of Coal Conversion, Institute of Coal Chemistry, Chinese Academy of Sciences, Taiyuan 030001, People's Republic of China

<sup>§</sup>BASF SE, 67056 Ludwigshafen, Germany

## Supporting Information

**ABSTRACT:** We have studied nucleation and crystal growth of calcium carbonate on hard surfaces, i.e. stainless steel and silica, at different temperatures, in relation to the corresponding bulk processes, using scanning electron microscopy (SEM), X-ray diffraction (XRD), and ellipsometry. In the bulk solution, a mixture of all three calcium carbonate crystalline polymorphs, calcite, aragonite, and vaterite, as well as amorphous particles was observed at 25 °C, while at 55 °C aragonite and calcite crystals dominated. On surfaces only calcite crystals were observed at 25 °C, whereas aragonite and calcite crystal adsorbed on the surfaces at 55 °C. Two kinds of nucleation and adsorption mechanism of  $\text{CaCO}_3$  crystals on hard surfaces were observed, depending on the surface orientation (vertical or horizontal, i.e., subject to sedimentation) in the bulk solution. A model for the relation between interfacial layer structure, the substrate, and the solution crystallization is discussed based on the observed difference in deposition between type of surfaces and surface orientation. In addition, the effect of magnesium ion on the morphology of calcium carbonate crystals is discussed.

**KEYWORDS:** calcium carbonate, surface deposition, calcite, nucleation, ellipsometry, scanning electron microscopy



## 1. INTRODUCTION

Calcium carbonate is one of the most common and widely spread minerals, occurring as limestone, chalk, and also in biominerals. It is widely used in industry as a raw material for cement, paper coating, medicine, etc., as it is harmless, cheap, and abundant. Unfortunately it is also readily formed where it is not wanted, for instance as scales on walls of heat exchangers and pipes and on the surface of dishes and cutlery in automatic dishwashers. Thus, a fundamental understanding of the crystal growth of calcium carbonate is not only relevant for inorganic chemistry, geochemistry, and biominerization, but also for a range of applications in areas such as chemical industries, cleaning, water treatment, and biotechnology processing. In practice, crystalline  $\text{CaCO}_3$  occurs in three polymorphs: calcite, aragonite, and vaterite, where calcite is the most thermodynamically stable and vaterite is the least stable.<sup>1,2</sup>

The formation of crystals and transformations between different  $\text{CaCO}_3$  polymorphs has been thoroughly investigated.<sup>3–8</sup> Many of these studies have been concerned with the physicochemical experimental conditions that control the formation and transformation of each of the three polymorphs of  $\text{CaCO}_3$ , including the effect of the reactant concentrations, mixing temperature, ionic strength, pH of the medium, and incubating time as well as the effect of inorganic/organic additives.<sup>9–12</sup> The temperature plays a particularly important role in the formation and transformation of the calcium

carbonate crystals. Wray and Daniels,<sup>13</sup> who studied the calcium carbonate polymorphs formed from highly supersaturated solutions of calcium carbonate, reported that aragonite was the predominant precipitate at high temperature (70 °C) and vaterite at low temperature (30 °C). Takeshi et al.<sup>14</sup> concluded that the amorphous calcium carbonate initially formed is transformed to a mixture of several crystalline  $\text{CaCO}_3$  polymorphs within several minutes. The polymorphs vaterite and calcite were formed at low temperature (14–30 °C), while aragonite and calcite were formed at high temperature (60–80 °C), and all three polymorphs formed at temperatures 40–50 °C. The formation of aragonite at higher temperatures was attributed to a decrease in supersaturation conditions.<sup>10</sup> Higher temperatures were also reported to increase the aspect ratio of the precipitated crystals.<sup>11</sup> Although nucleation and growth mechanisms, as well as the kinetics of calcium carbonate formation have previously been studied, significantly less is known about the  $\text{CaCO}_3$  crystal formation/deposition mechanism on a solid surface. Yamanaka et al.<sup>15</sup> studied the heterogeneous nucleation and crystal growth of  $\text{CaCO}_3$  on mica surface and on highly oriented pyrolytic graphite (HOPG) substrate by AFM technique. They found that the initial growth

**Received:** August 13, 2012

**Accepted:** April 18, 2013

**Published:** April 18, 2013



process can be divided in three stages: the amorphous, the intermediate, and the crystalline stage. The heterogeneous nucleation of calcium carbonate is believed to be controlled by the electrostatic interaction between the hydrated calcium ion and the substrate. The  $\text{CaCO}_3$  deposition on solid surface and the effect of inhibitor addition have been studied with a range of techniques,<sup>16–19</sup> including electrochemical technique combined with a quartz crystal microbalance method.<sup>20–23</sup> However, so far the relationship between bulk precipitation and surface  $\text{CaCO}_3$  formation has received little attention, in particular how the temperature affects the  $\text{CaCO}_3$  deposition mechanism on hard surfaces.

The aim of this study is to reveal the effect of temperature on the formation and transformation processes of calcium carbonate deposition on different hard surfaces in relation to precipitation in the bulk solution. In particular we will focus our discussion on the precipitation and deposition at pH 10, as automatic dishwashers for a household usually operate at this pH during the wash cycle. Our goal in this respect is to provide knowledge that can lead to processes and detergents that give less deposition. One important aspect is to determine whether the calcium carbonate particles are deposited by sedimentation or the crystals are formed on the surface, i.e. if the surface acts as nucleation site. For this purpose the effect of surface orientation, vertical versus horizontal, where the surface is subject to deposition from sedimentation of particles, on the structure and morphology of  $\text{CaCO}_3$  crystal has been determined. Furthermore, the effect of surface properties on the process was determined. Here three types of surfaces were used: smooth silicon wafers, one that has been acid cleaned in the final step (less deprotonated OH-groups) and the other that was alkaline treated (expected to have a more negative charge), and finally a more rough stainless steel surface, expected to provide more nucleation sites for the crystals on the surface. A null ellipsometer was used to *in situ* follow the adsorption kinetics and adsorbed amount of  $\text{CaCO}_3$  particles on the surface. The particles were characterized with scanning electron microscope (SEM), energy dispersive X-ray spectroscopy (EDS), and X-ray diffraction (XRD).

## 2. EXPERIMENTAL SECTION

**2.1. Preparation of  $\text{CaCO}_3$  Crystal from Hard Water.** The following chemicals were purchased and used without further purification:  $\text{CaCl}_2$  (Sigma-Aldrich),  $\text{MgCl}_2$  (anhydrous, >98%, Sigma),  $\text{NaHCO}_3$  (Merck, >99.5%),  $\text{Na}_2\text{CO}_3$  (Sigma-Aldrich, >99%). Milli-Q water was used for the preparation of the hard water and other solutions. Hard water was prepared by adjusting the hardness of the water to 21° dH by adding 4 mM  $\text{Ca}^{2+}/\text{Mg}^{2+}$  (4:1) + 8 mM  $\text{HCO}_3^-$ , and pH was set to 10 using  $\text{Na}_2\text{CO}_3$ . For this purpose, stock solutions of  $\text{CaCl}_2$ ,  $\text{MgCl}_2$ ,  $\text{NaHCO}_3$ , and  $\text{Na}_2\text{CO}_3$  with concentrations of 0.5, 0.1, 0.5 M, and 1 M, respectively, were used.  $\text{CaCO}_3$  crystals precipitated from solution by quick addition of concentrated solutions of  $\text{NaHCO}_3$  into a beaker containing aqueous solutions of  $\text{CaCl}_2$  and  $\text{MgCl}_2$  at two reaction temperatures of  $25 \pm 0.2$  and  $55 \pm 0.2$  °C, respectively. The temperature was controlled using a water bath, and the pH was adjusted to a value of 10 by  $\text{Na}_2\text{CO}_3$  solution. During mixing, pH adjustments, and crystal formation, the solution was stirred at a constant rate of 300 rpm using a magnetic stirrer. After different reaction times, ranging from 1 min to 15 h, particles were collected by centrifugation (5000 rpm and 10 min), followed by filtration through filter funnel (glass, 0.45 µm). The particles were subsequently rinsed three times with Milli-Q water and then dried in the oven at 50 °C for at least 24 h. The particles were characterized by scanning electron microscopy (SEM), energy dispersive X-ray spectroscopy (EDS), and X-ray diffraction (XRD).

**2.2. Surface Preparation and Treatment.** Three types of surfaces were chosen as substrates: stainless steel surface (304), acid treated silica surface, and alkali treated silica surface. The silica surfaces (p-type, boron doped) were thermally oxidized in an oxygen atmosphere at 920 °C for 1 h, followed by annealing and cooling in an argon flow. This procedure yields a 300 Å thick  $\text{SiO}_2$ . The oxidized wafers were cleaned in a mixture of (1) 25%  $\text{NH}_4\text{OH}$ , 30%  $\text{H}_2\text{O}_2$ , and water (1:1:5 by volume) at 80 °C, (2) followed by boiling for 10 min in a mixture of concentrated hydrochloric acid, 30%  $\text{H}_2\text{O}_2$ , and water (1:1:5 by volume) at 80 °C for acid treated silica wafer, and 1–2–1 for the alkali treated silica wafer. Finally, the cleaned oxidized wafers were stored in ethanol for SEM and ellipsometry measurements. The stainless steel surfaces were cleaned using the alkali detergent, Decon 90, at a concentration of 2 wt %. In order to obtain the layer deposition, the silica or stainless steel plate was immersed into hard water with horizontal (surface subject to sedimentation) or vertical orientation. Then, the stock solution of concentrated  $\text{NaHCO}_3$  and  $\text{Na}_2\text{CO}_3$  were quickly added. The sample plate was taken out of the solution after different equilibration times, quickly rinsed with purified water to remove any residual salt solution, and then dried in a closed, dust-free container. SEM and atomic force microscope (AFM) were then used to analyze the samples, which had been exposed to the calcium carbonate solution for different times.

**2.3. Experimental Methods.** An automated Rudolph Research thin-film null ellipsometer, type 43603-200E, was used to measure (*in situ*) the adsorbed amount and the thickness of the adsorbed layers. The method is based on measurements of the change of polarized light in terms of the relative phase shift,  $\Delta$ , and the relative change in amplitude,  $\Psi$ , upon reflection against an interface.<sup>24</sup> On the basis of these data and the optical properties of the substrate, the refractive index,  $n_b$ , and the film thickness,  $d_f$ , of the deposited layer can be determined.<sup>25,26</sup> The approach used to determine the properties of the used silicon substrate with a 300 Å thick oxide layer is described by Landgren and Jönsson.<sup>27</sup> The stainless steel surface was considered to be an homogeneous substrate without any oxide layer. The adsorbed amount was calculated using the formula of de Feijter et al.:<sup>28</sup>

$$\Gamma = \frac{d_f(n_f - n_0)}{dn/dc}$$

where  $dn/dc$  is the refractive index increment of the calcium carbonate (0.1 mL/g)<sup>29</sup> and  $n_0$  is the refractive index of the ambient bulk solution. It should be noted that ellipsometry signal is sensitive to changes in the dielectric properties of an adsorbed layer independent of whether the layer is homogeneous or not. The data from ellipsometry measurements is evaluated assuming a homogeneous layer. Therefore the thickness extracted from such a model represents some optical average thickness, which does not necessarily represent the physical thickness of the adsorbed layer in particular at low surface coverage. Different models, like the Bruggeman effective medium expression, can be used to calculate a mean refractive index and corresponding thickness as discussed previously.<sup>26</sup> However it has been shown that the calculated value of the adsorbed amount from the refractive index and the thickness of the layer is not as dependent on the optical model and can be used for inhomogenous layers as verified by other methods (cf. refs 30 and 31). Another concern is the fact that crystals of  $\text{CaCO}_3$  are birefringent, and this can potentially affect the ellipsometry reading. However to do so the crystals need to be of the same size as the area illuminated during the measurement, e.g. in the order of several squared millimeters, or if significantly smaller they should be ordered with their optical axis in the same direction. The SEM images show that the crystals are in the micrometer range and deposited/formed randomly on the surface with no particular orientation, and therefore, the birefringence of individual crystals will not affect the ellipsometry results. All measurements were performed at a wavelength of 401.5 nm and an angle of incidence of 68.5°. A 5 mL thermostatted cuvette was used for the *in situ* measurements at 25.0 °C or other temperatures. The solution in the cuvette was agitated with a magnetic stirrer at about 300 rpm.

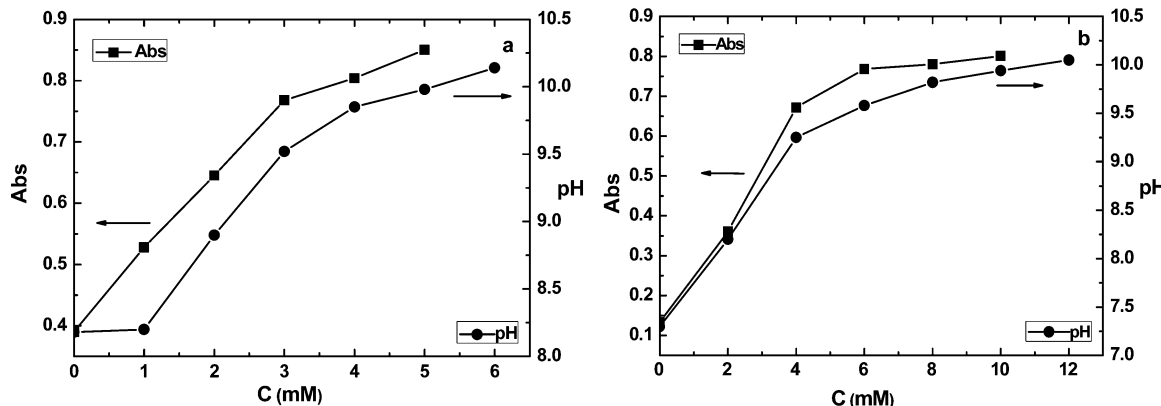
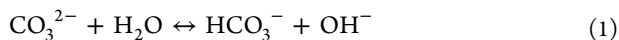


Figure 1. Turbidity and pH value of  $\text{CaCO}_3$  solution at different concentrations of  $\text{Na}_2\text{CO}_3$ : (a) 25 and (b) 55 °C.

The deposited  $\text{CaCO}_3$  particles were characterized by SEM (JEOL JSM-6700F), X-ray diffraction (XRD), and AFM (Digital Instruments, Nanoscope III, tapping mode). All samples were Au-coated prior to the SEM investigation. The SEM was fitted with a field emission source and operated at an accelerating voltage of 5.0 kV. Energy dispersive X-ray spectroscopy (EDS) was used to determine the composition of crystals and the spectra was measured in the SEM instrument with an Oxford Instruments INCA Microanalysis. The XRD measurements were conducted using a Rigaku D/max-2400 powder X-ray diffractometer with  $\text{Cu K}\alpha$  radiation (40 kV, 120 mA), and 0.02 step and  $2\theta$  range of 20–60° were selected to analyze the crystal structure and type. Dynamic light scattering (DLS) and Zeta potential measurements (Zetasizer Nano, Malvern) was used to estimate the particle size and charge in the solution. The kinetics of the bulk aggregation was followed by measuring the turbidity of the solution, using a UV-vis spectrometer (Perkin-Elmer LS-50B spectrometer, at a wavelength 500 nm). The X-ray diffraction peaks at  $2\theta = 29.4^\circ$ ,  $26.2^\circ$ , and  $27.0^\circ$  for calcite (104), aragonite (111), and vaterite (112), respectively, were used to calculate the polymorphic ratio of the polymorphs in the precipitated  $\text{CaCO}_3$ . The content of each polymorph was calculated from the diffraction peak height using a calibration curve obtained from crystal mixtures with known ratios of the polymorphs. These values obtained from the peak height are in agreement with those obtained from the peak area reported previously.<sup>14,32</sup>

### 3. RESULTS

**3.1. Kinetics of  $\text{CaCO}_3$  Precipitation in the Bulk Solution.** The turbidity and pH value of hard water as a function of  $\text{Na}_2\text{CO}_3$  concentration were obtained by titrating  $\text{Na}_2\text{CO}_3$  into hard water under agitation. The results which represent the total amount of particles are presented in Figure 1 and show that about 5 mM  $\text{Na}_2\text{CO}_3$  at 25 °C and 10 mM at 55 °C is needed to obtain a pH value of 10 of the  $\text{CaCO}_3$  solution. The turbidity under these conditions is quite high, suggesting formation of  $\text{CaCO}_3$  particles. The change of pH value of hard water at different temperatures can be described by the following equilibria.



The mean values of the  $\text{CaCO}_3$  solubility product ( $K_{\text{SP}}$ ) were found to be  $4.7 (\pm 0.3) \times 10^{-9}$  at 25 °C and  $2.6 (\pm 0.3) \times 10^{-9}$  at 55 °C, and an increase of temperature is expected to promote  $\text{CaCO}_3$  precipitation.<sup>8,14</sup> As apparent from formula 1 and 2, an increase of precipitation will decrease the pH value of the solution. In order to keep the pH at 10, more  $\text{Na}_2\text{CO}_3$  had to be added at 55 °C. The molar ratio of  $\text{Ca}^{2+}/\text{CO}_3^{2-}$  is 1:1.2 at

25 °C and 1:2.5 at 55 °C, which means that the solution is a supersaturated mixture.

Here it is important to note that any change in turbidity reflects both nucleation and growth of particles. The particle size distribution is a result of the competition between these both processes. In general this leads to a rather wide size distribution, which is challenging to measure with e.g. DLS. However, since the larger particles sediment to the bottom of the sample cell rather rapidly we can get an estimation of the nucleation process by performing kinetic measurement without agitation. We therefore measured the turbidity (shown as absorbance in Figure 2) as a function of time at different

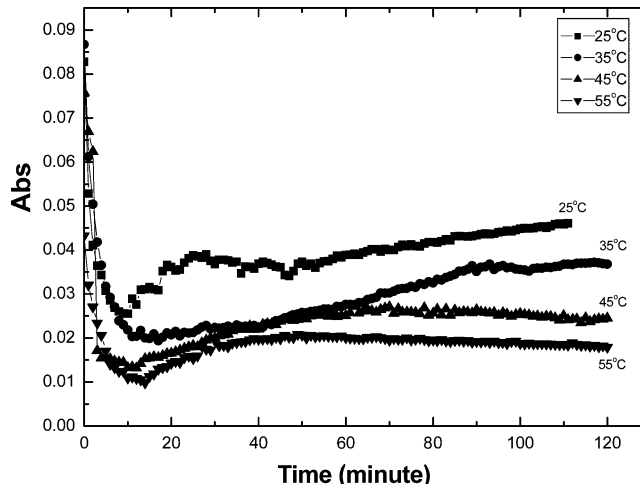


Figure 2. Turbidity (shown as absorbance) caused by  $\text{CaCO}_3$  precipitation from hard water as a function of time at different temperatures. The data is recorded without agitation, allowing larger particles to sediment.

temperatures, 25, 35, 45, and 55 °C, respectively. The turbidity of solutions remained at a high value immediately after adding  $\text{Na}_2\text{CO}_3$  stock solution during agitation. After the addition of  $\text{Na}_2\text{CO}_3$ , the agitation was stopped and the change in turbidity was followed as a function of time without stirring the solution. The absorbance for the different temperatures initially decreased steeply with time as the precipitate settled in the cuvette. Eventually, after about 15 min, the turbidity reaches a low steady-state value, which shows that most of the precipitate from the solution will settle fast at the bottom of the cuvette. However, we observed that the settling time, i.e. the time

required to form aggregates large enough to sediment depends on temperature. In fact, the time required until the turbidity reaches the lowest value increases with the temperature. For instance it takes 8 min at 25 °C while it takes 14 min at 55 °C to reach steady state turbidity. Furthermore, the steady state value of the turbidity of the solution (after 1 h) decreased systematically with increasing temperature of the solution. This indicates that there are fewer and/or finer particles dispersed in the solution at higher temperature after sedimentation. This effect was further investigated using DLS, and the results for 25 °C are shown in Supporting Information Figure S1.

The DLS data show that particles in the supernatant are finely dispersed with a rather narrow size distribution and particle sizes of only a few hundred nanometers. It addition, the temperature has a strong influence on the particle size, where particles formed at 25 °C are about twice as large as those prepared at 55 °C, while there is only a minor influence on the size distribution.

It is important to note that most of the particles formed settled to the bottom in a very short time, and therefore, only a fraction of very small particles exhibit sufficient colloidal stability to remain dispersed in the solution after 3 h. The zeta potential of these CaCO<sub>3</sub> particles was found to be  $-30 \pm 3$  and  $-35 \pm 3$  mV, for 25 and 55 °C, respectively. The temperature at which the particles are formed does not affect the zeta potential significantly, and the magnitude is a reasonable value for a stable colloidal dispersion. An interesting feature of the turbidity (results shown in Figure 2) is that there appears to be a minima in turbidity, again reflecting the competition between the nucleation and the growth processes. For the lower temperature, no plateau value is observed after long equilibrium times, while at the higher temperatures, a plateau is reached. If we consider the fact that DLS shows that smaller particles are formed at the higher temperature, it is tempting to suggest that the nucleation process is more pronounced at higher temperature and that, at the plateau value, the solution is no longer supersaturated. At the lower temperature, fewer nuclei are formed and the growth of the particles is stronger giving higher turbidity.

The effect of temperature on reversibility of CaCO<sub>3</sub> precipitation from hard water under agitation is shown in Figure 3. When the pH value of hard water is 10, the solution is somewhat turbid already at 25 °C and the turbidity increases

with temperature, which indicates that more CaCO<sub>3</sub> precipitate is produced in the solution at high temperature. But when the temperature goes back from 55 to 25 °C, the turbidity remains constant. We can conclude that high temperature will promote the formation and growth of particles, but the process is irreversible and the produced particles will not redissolve when the temperature again decreases.

### 3.2. Kinetics of CaCO<sub>3</sub> Deposit Formation on Solid Surfaces.

The bulk of the studies were conducted under conditions, which mimic the ADW (automatic dishwasher) conditions, namely pH 10 and with hard water (21°dH, 4 mM Ca<sup>2+</sup>). Unfortunately these conditions create turbid solutions, which makes kinetic studies using ellipsometry a challenge. To get information about in situ kinetics of crystal deposition, ellipsometry is used to study the crystal deposition/formation under conditions of low turbidity (low concentration of CaCO<sub>3</sub>, 2 mM, and lower pH 9.3 instead of 10). Under these conditions, the calcium carbonate deposition/formation is expected to be more reversible. The amount of CaCO<sub>3</sub> on the silica surfaces is rather small, but still some crystals remain after dilution (0.02 mg/m<sup>2</sup>) close to the detection limit of our ellipsometry setup. For stainless steel surfaces on the other hand significantly larger amounts are observed and the deposition seems to be irreversible upon dilution as indicated in Figure 5. With respect to the SEM and AFM images recorded, we note that these reflect the firmly attached crystals. The short rinsing step applied was used to avoid the artifact due to deposition from drying the CaCO<sub>3</sub> solution. The rinsing step during the ellipsometry measurements was significantly longer and involved the use of a larger volume of water (about 20 times more). Figure 4 gives a typical example of the time dependence of the adsorbed amount of CaCO<sub>3</sub> from hard water on two kinds of silica surfaces at pH 9.3. As shown in Figure 4a, the adsorption kinetics observed is slow, and the adsorbed amount initially increases linearly with time. The adsorbed amount did not approach an apparent plateau value even after approximately 3 h for the acid treated silica surface. However, for alkali treated silica surface (results shown in Figure 4b), the value of adsorbed amount increases initially with time, and then reaches an apparent plateau after 1.5 h. When the CaCO<sub>3</sub> solution was diluted with continuous rinsing with pure water (indicated by the arrows in Figure 4a and b), complete desorption occurred within a few minutes from both of these two surfaces. The adsorption mechanism can be thought of either as build-up of crystals at the surface or as attachment of crystals to the surface. At this stage we cannot discriminate between the two modes of creating the surface deposits, but we will get more details about the adsorption mechanism by SEM images, which will be discussed in more detail below. We also note that the adsorbed amount at the acid treated silica surface is larger than that at the alkali treated silica surface, even though the amount adsorbed on both of them are fairly low. Since preliminary SEM data revealed that significantly higher amounts of crystals are adsorbed on the stainless steel surface, this type of surface was used for further ellipsometry studies. Figure 5 shows the adsorbed amount as a function of temperature with 2 mM Na<sub>2</sub>CO<sub>3</sub> (about pH 9.3) on stainless steel. From Figure 5, it is apparent that the adsorbed amount of CaCO<sub>3</sub> on the steel surface at 25 °C is higher than that on the silica surface. This can possibly be due to the fact that the steel surface is rougher. There is a sharp decrease in the adsorbed amount with increasing temperature from 25 to 40 °C, and the amount then slowly decreases until 55 °C reached.

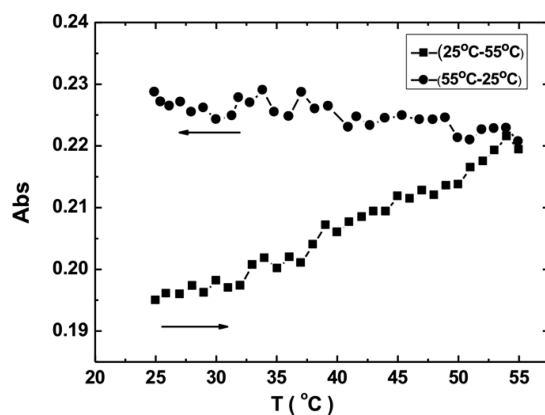


**Figure 3.** Turbidity (plotted as absorbance) of CaCO<sub>3</sub> at different temperature (from 25 to 55 to 25 °C) and pH = 10. The data given is recorded after equilibrating at each temperature for 5 min under agitation.

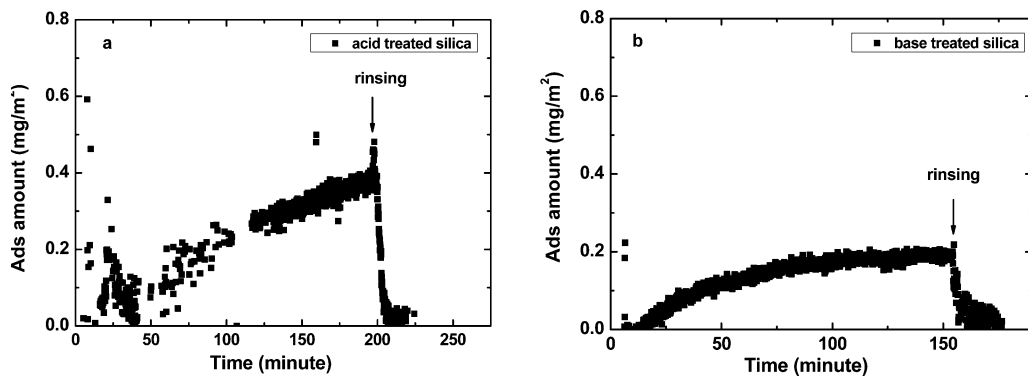


**Figure 4.** Adsorbed amount of  $\text{CaCO}_3$  particle on the silica surfaces as a function of time with 2 mM  $\text{Na}_2\text{CO}_3$  at 25 °C and pH 9.3: (a) acid treated silica, (b) alkali treated silica.

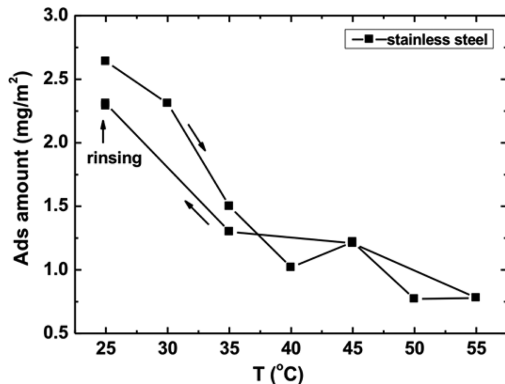


**Figure 5.** Adsorbed amount of  $\text{CaCO}_3$  particle on the surface of stainless steel as a function of temperature with 2 mM  $\text{Na}_2\text{CO}_3$  and pH 9.3 as determined by ellipsometry.

When the temperature goes back from 55 to 25 °C, the adsorbed amount on the surface will increase again. After

rinsing with pure water, the adsorbed amount does not change, which indicates that there is strong adsorption of  $\text{CaCO}_3$  on the steel surface. It can also be concluded that higher temperatures will give rise to desorption of particles from the steel surface, and in this respect, the adsorption appears reversible.

**3.3. Crystal Morphology and Structure in the Bulk Solution.** Typical SEM images of calcium carbonate crystals formed after various equilibration times at 25 °C are shown in Figure 6. All three crystalline polymorphs and amorphous particles are observed when the reaction time is 1 min (Figure 6a), which is verified by the X-ray diffraction results (Figure 7). The amorphous  $\text{CaCO}_3$  (ACC) small spherical particles with diameters of about 0.1  $\mu\text{m}$  appear to be metastable and aggregate into larger spherical particles (about 10  $\mu\text{m}$ ). During this stage, the spherical vaterite crystal (about 1  $\mu\text{m}$ ) and rhombohedral calcite are the predominant polymorphs, and quite a few needlelike aragonite crystals are observed. The corresponding XRD pattern recorded after 1 min at 25 °C showed weak peaks from aragonite crystals in addition to the sharp peaks from calcite and vaterite. On the basis of the area

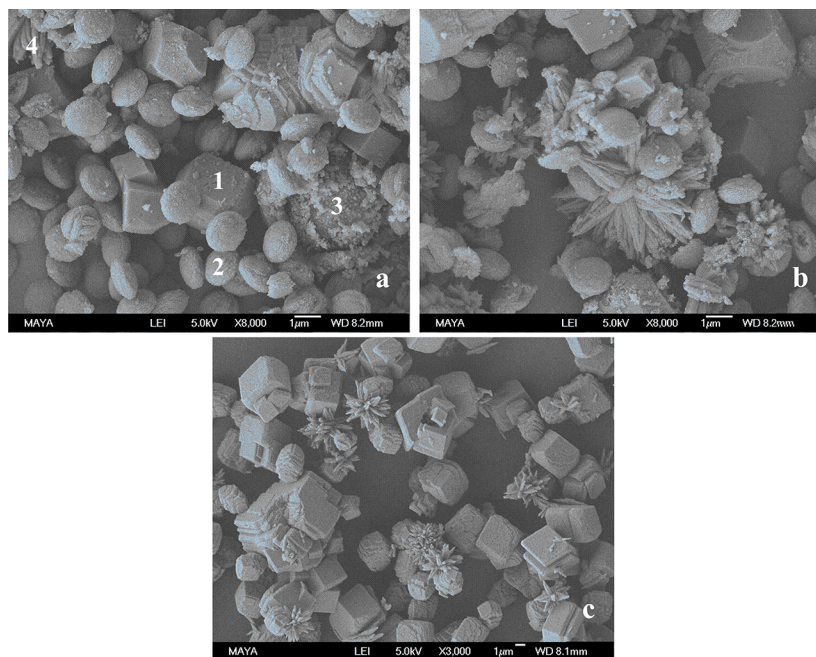


**Figure 6.** SEM images of  $\text{CaCO}_3$  crystal in the bulk solution after different time at  $T = 25$  °C and pH 10: (a) 1 min, (b) 1 h, and (c) 15 h. The numbers 1, 2, 3, and 4 in part a represent calcite, vaterite, amorphous, and aragonite, respectively.

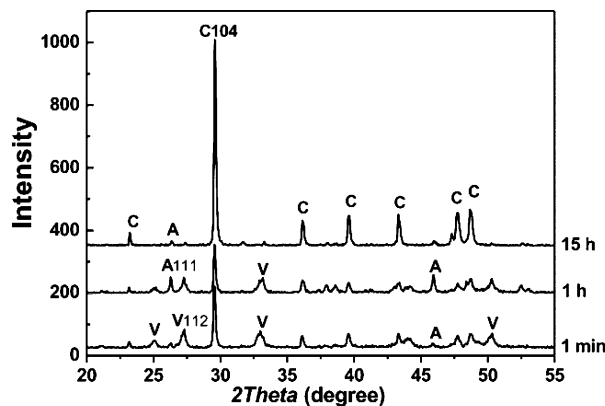


**Figure 7.** XRD patterns of  $\text{CaCO}_3$  obtained at pH 10 and  $25\text{ }^\circ\text{C}$ . A, V, and C denote diffraction peaks assigned to aragonite, vaterite, and calcite, respectively.

under the peaks, the sample contains about 5 wt % aragonite, 73 wt % calcite, and 22 wt % vaterite (Table 1). Figure 6b

**Table 1. Relative Composition Polymorphs in  $\text{CaCO}_3$  Crystals Obtained by Integrating the XRD Peak Areas for Samples Equilibrated at 25 and  $55\text{ }^\circ\text{C}$**

time (temp)	content of crystal polymorphs (wt %)		
	calcite	aragonite	vaterite
1 min ( $25\text{ }^\circ\text{C}$ )	$73.0 \pm 0.5$	$5.0 \pm 0.5$	$22.0 \pm 0.5$
1 h ( $25\text{ }^\circ\text{C}$ )	$59.0 \pm 0.5$	$20.0 \pm 0.5$	$21.0 \pm 0.5$
15 h ( $25\text{ }^\circ\text{C}$ )	$92.0 \pm 0.5$	$8.0 \pm 0.5$	0
10 min ( $55\text{ }^\circ\text{C}$ )	$9.0 \pm 0.5$	$91.0 \pm 0.5$	0
15 h ( $55\text{ }^\circ\text{C}$ )	$30.0 \pm 0.5$	$70.0 \pm 0.5$	0

shows that the amorphous particles and vaterite particles progressively disrupt into small particles with time during the course of the polymorphic transformation. The calcite crystals simultaneously grow larger with first rough surface, but once

steady state is approached (after 15 h) the crystals appear smoother. The XRD results also showed that the relative amount of aragonite seems to increase with time (20 wt % after 1 h), while the content of calcite and vaterite decreased slightly to 59% and 21%, respectively. This suggests that most of the amorphous  $\text{CaCO}_3$  and some vaterite crystal transformed to aragonite, which also is confirmed by SEM results. Finally after 15 h, all amorphous  $\text{CaCO}_3$  particles and vaterite crystals have disappeared (Figure 6c) and transformed into calcite and aragonite. The corresponding XRD results (Figure 7) confirm that calcite is the dominant crystalline phase with a minor fraction of aragonite (8 wt %) and no vaterite. The SEM images show that all amorphous particles and vaterite crystals transformed to calcite or aragonite. Most of the aragonite is also transformed to calcite. It is known that this transformation is not a direct solid phase conversion but a recrystallization of calcium carbonate through the dissolution of vaterite and the growth of calcite or aragonite.<sup>14</sup> Since the growth rate of calcite is much slower than the dissolution rate of vaterite, the rate-determining step of the transformation of vaterite to calcite is the growth of calcite.<sup>14</sup>

The polymorphs of  $\text{CaCO}_3$  crystals formed at  $55\text{ }^\circ\text{C}$  are quite different from those obtained at  $25\text{ }^\circ\text{C}$ . From SEM images (Figure 8), it can be concluded that (a)  $\text{CaCO}_3$  crystals in all samples form two types of crystals, namely aragonite and calcite, which is in agreement with XRD results (Figure 9). The calcite crystal has a distorted cubic morphology, and aragonite crystal has several different morphologies, such as leaflike, needlelike, and flowerlike shapes. The crystal size is quite polydisperse, ranging from 1 to  $10\text{ }\mu\text{m}$ . Aragonite crystals dominate in all the samples, while the content of calcite crystal is quite small in the initial stage and gradually increases with time. The XRD results also showed that sample contains about 9 and 91 wt % calcite and aragonite, respectively in the initial stage (10 min), and the corresponding value after 15 h is 30 and 70 wt %, respectively. This means that either more

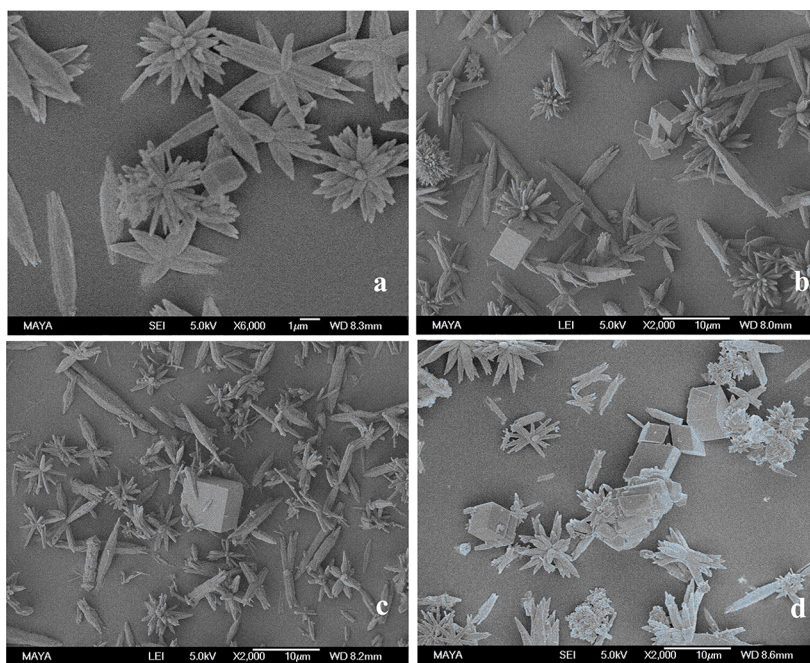


**Figure 8.** SEM images of calcium carbonate crystal recorded versus time at  $T = 55\text{ }^\circ\text{C}$  and pH 10: (a) 10 min, (b) 1 h, (c) 5 h, and (d) 15 h.

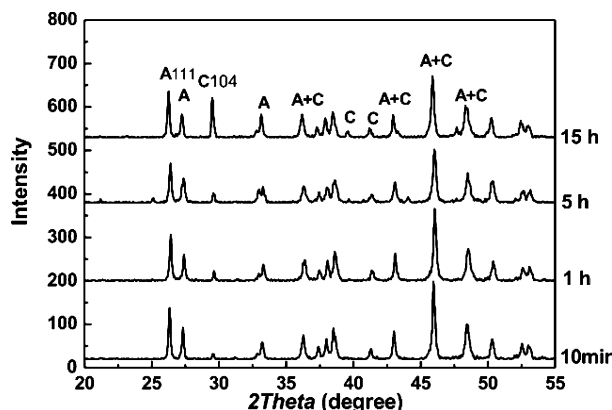


**Figure 9.** XRD pattern of  $\text{CaCO}_3$  crystal obtained at  $55\text{ }^\circ\text{C}$  and pH 10. A and C denote peaks from aragonite and calcite, respectively.

ragonite crystals transformed to calcite crystal or more calcite crystals are formed with time.

**3.4. Effect of  $\text{Mg}^{2+}$  on the Morphology of  $\text{CaCO}_3$  Crystal.** To analyze the composition of  $\text{CaCO}_3$  crystal, we performed energy dispersive X-ray spectroscopy (EDS) measurements using the same samples (10 min and 15 h) as in the XRD and SEM measurements at  $T = 55\text{ }^\circ\text{C}$  and pH 10. From the results summarized in Table 2, the following can be

**Table 2. EDS Results of  $\text{CaCO}_3$  Crystals Obtained from the Saturated Bulk Solution after 10 min and 15 h at  $T = 55\text{ }^\circ\text{C}$  and pH 10**

time	content of $\text{CaCO}_3$ , Na, or Mg in crystal polymorphs (wt %)	
	calcite	aronite
10 min	$\text{CaCO}_3$ : 100	$\text{CaCO}_3$ : 100
15 h	$\text{CaCO}_3$ : 99.2 Mg: 0.8	$\text{CaCO}_3$ : 98.8 Na: 0.4

conclude: (a) Aragonite crystals do not contain Mg and only small amounts of Na after 15 h. (b) The Mg content in the calcite crystals depends on the incubation times; for sample 1, incubated for 10 min, the crystals are very small and there is no Mg in the crystal, while for sample 2, incubated for 15 h, the crystals are larger and contain small amounts of Mg. Hence no Mg is incorporated in the initial stage of calcite crystal formation, but Mg seems to be incorporated during the crystal growth, which appears to affect the crystal shape and growth process.

This study also shows that homogeneous  $\text{CaCO}_3$  crystals are formed in the initial stage of calcite formation and that the calcite crystals are rhombohedral crystals.  $\text{Mg}^{2+}$  ion adsorption on the calcite leads to a heterogeneous Mg– $\text{CaCO}_3$  surface and distorted calcite crystals. Typically calcite crystal surfaces are classified as F (flat), S (stepped) and K (kinked) surfaces,<sup>33,34</sup> as shown in Figure 10. Normally, the K and S surfaces are absent in equilibrium crystal morphologies. The new crystal faces start to appear in the presence of  $\text{Mg}^{2+}$  on the edges or corners of the original surfaces of rhombohedral calcite seed crystals (shown in Figure 10). Paquette and Reeder<sup>35</sup> suggest that there are geometrically different types of surface sites on the original surfaces of the calcite seeds. Mg<sup>2+</sup> has a higher affinity for some of these sites, i.e. K surfaces, and adsorption of the ion or perhaps dehydration during Mg<sup>2+</sup> incorporation that slows down crystal growth in specific directions, for example

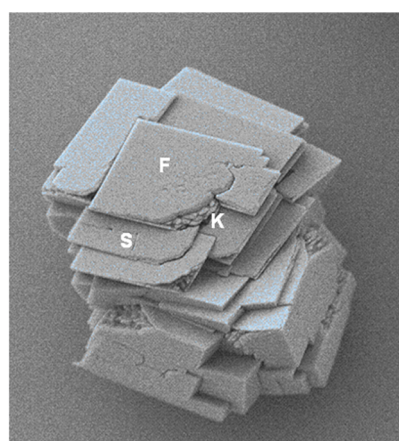


**Figure 10.** SEM image of a calcite crystal illustrating F (flat), S (stepped), and K (kinked) surfaces.

toward the edges and corners. As a consequence of inhibition by  $\text{Mg}^{2+}$ , new crystal faces will develop and the crystals become more distorted.

**3.5. Crystal Morphology of Calcium Carbonate on Hard Surfaces.** The surface properties of the substrate play a crucial role in determining which type of calcium carbonate particles are adsorbed/formed at a solid surface.<sup>36</sup> Thus, it is important to characterize, e.g., the calcium carbonate particle size and shape both formed in bulk and on the substrates in order to relate precipitation to the particle adsorption. The morphology of  $\text{CaCO}_3$  on different hard surfaces was studied by SEM measurements at 25 and  $55\text{ }^\circ\text{C}$ , respectively. In addition, the effect of surface orientation, horizontal and subject to sedimentation versus vertical, on the structure and morphology of  $\text{CaCO}_3$  deposits were also investigated. Representative images for horizontal and vertical orientation of the sample at 25 and  $55\text{ }^\circ\text{C}$  recorded after 1 h for stainless steel and base treated silica surfaces are shown in Figures 11 and 12, respectively. The time dependence of the process for these surface as well as acid treated silica is shown in the Supporting Information in Figures S2–S7. From the SEM images it can be concluded that there are two dominating types of crystal forms on the surfaces, namely rhombohedral and staircaselike calcite. This indicates that the calcite crystals are more likely to adhere/form on the surface than are the other polymorphs. The staircaselike crystals on the horizontal surface are about  $10\text{ }\mu\text{m}$ , which is almost the same size as those formed in the bulk solution. This suggests that these crystals precipitate from bulk solution and sediment on the surface, while the small defective particles are likely to nucleate and form on the surface. In addition, the amount of crystal on the surface increased with incubation time (see Figure S2–S7). The calcite crystals formed at a vertical orientation of the surface, where sedimentation on the surface does not occur (Figure 11d and 12d), are significantly smaller (less than  $1\text{ }\mu\text{m}$ ), and some are not completely rhombohedral. These results suggest that these tiny crystals are surface nucleated and grew by the direct crystallization from ions in solution. In addition, the number of crystals on a vertical surface is significantly lower than that on a horizontal surface.

The SEM images of  $\text{CaCO}_3$  on the alkali treated silica surface are shown in Figure 12. These images are qualitatively similar to those of the stainless steel surface exposed to the saturated  $\text{CaCO}_3$  solution. It should be noted though that the amount of

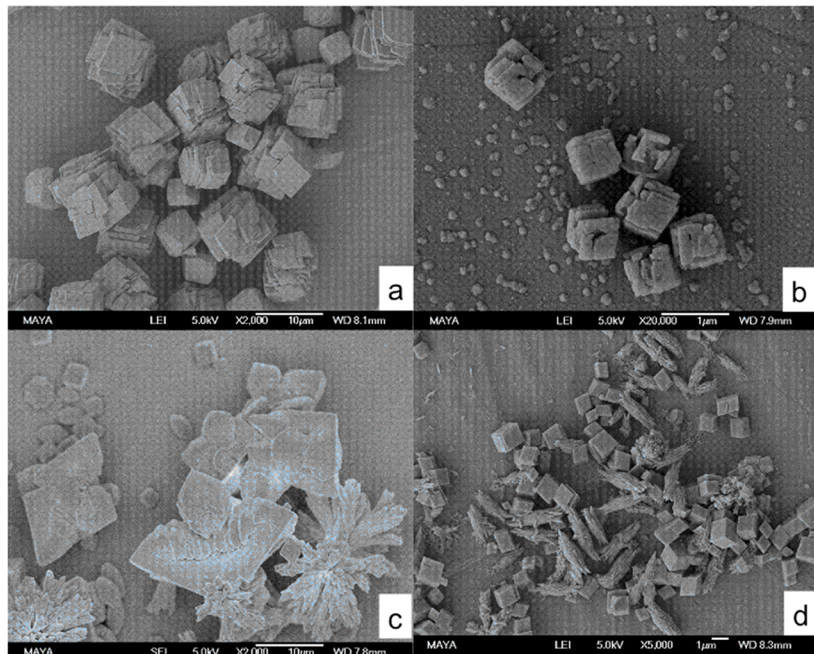


**Figure 11.** SEM images of  $\text{CaCO}_3$  crystal formation/deposition on the surface of stainless steel at  $T = 25$  (a, b) and  $55^\circ\text{C}$  (c, d) at pH 10 after 1 h. The horizontal surface orientation is in a and c, and the vertical surface orientation is in b and d.

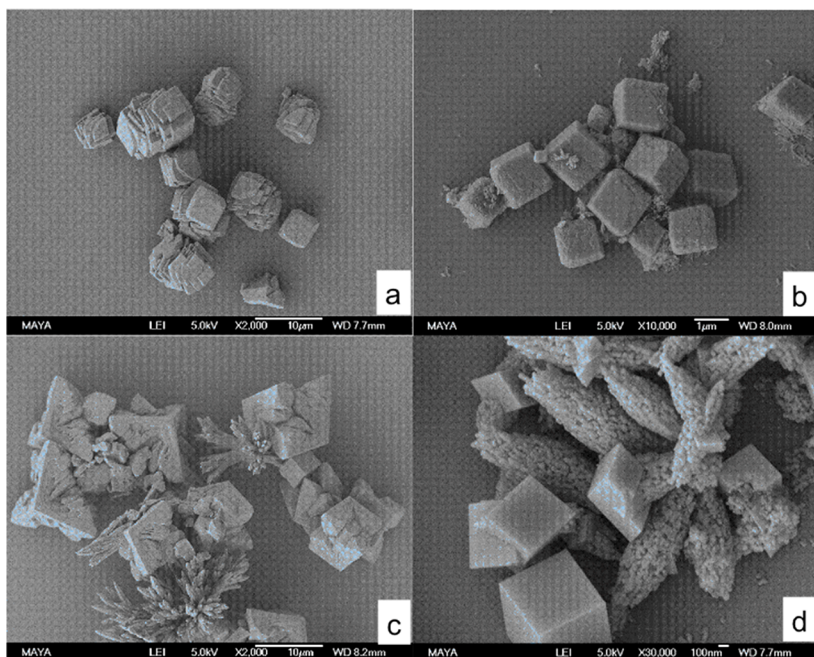


**Figure 12.** SEM images of  $\text{CaCO}_3$  crystal on the alkali treated silica surface at  $T = 25$  (a, b) and  $55^\circ\text{C}$  (c, d) at pH 10 for 1 h. The horizontal surface orientation is in a and c, and the vertical surface orientation is in b and d.

calcite on the surface in this case has increased significantly when the reaction time is 10 h (Supporting Information Figure S3). In addition, the calcite crystals on the vertical silica surface (Figure 12c and d) appear more typically rhombohedral and complete than particles on the steel surface in the vertical orientation (Figure 12d). The SEM images show that the amount of crystals is low on vertical alkali treated silica surface where most of the area on the surface is free of  $\text{CaCO}_3$  crystals. We did not observe any significant differences between SEM images of  $\text{CaCO}_3$  crystals on the acid treated silica surface (Supporting Information Figure S4) and the corresponding

images of alkali treated silica surfaces and stainless steel surfaces. However, the morphology of the crystals on the acid treated surface seems to contain more stairs.

The corresponding SEM images of  $\text{CaCO}_3$  crystal formation/deposition on hard surfaces at  $55^\circ\text{C}$  are shown in Figures 11c and d and 12c and d. The results for the stainless steel (SEM images in Figure 11c and d and Figure S5) show the following:

- (1) Calcite crystal dominates, and a significantly lower amount of aragonite is observed on the surface compared to precipitates from bulk solution (Figure 8). This means

- that calcite has a higher affinity or is more easily formed on the surface than aragonite. In addition, the shape of crystals obviously changes: the calcite crystals are not typically rhombohedral any more but incomplete and distorted rhombohedral, and the aragonite crystals have dumbbell–flowerlike shape.
- (2) The amount of particles formed/deposited on the surface increases with exposure time (Supporting Information Figure S5), and a lot of tiny crystals (of about 1  $\mu\text{m}$ ) appeared after 1 h (Figure 11c and d). Also at this higher temperature, the results indicate that there are two types of ways in which the crystals arrive to the surface. We suggest that large crystals, with size of about 10  $\mu\text{m}$  and almost the same as those in the bulk solution, are deposited directly from bulk solution. They are dominating on the horizontally oriented surface, which is subject to sedimentation. On the other hand, the small crystallites are suggested to nucleate and grow at the surface and they are dominating on the vertically oriented surface.
- (3) The typically rhombohedral calcite crystal is dominant on the surface of the sample oriented vertically and therefore not subject to sedimentation (shown in Figure 11d), and the morphology of aragonite is spindelike. In addition, the size of the crystal is around 1  $\mu\text{m}$ , and the adsorbed amount is significantly lower than on the horizontally oriented surface.

When the silica substrate is treated with alkali (Figure 12c and d), the crystals on the horizontal surface are a little bit different from those on the stainless steel surface. On the horizontally oriented alkali treated silica surface, the shape of calcite is more incomplete and distorted, and in contrast to the stainless steel surface, we do not see any tiny crystals. Here we note that the stainless steel surface is considerably rougher than the silica surface and might therefore provide more nucleation sites for growth of crystals on the surface. In addition, the crystals on vertical alkali treated surfaces are quite similar to those on the steel surface formed under corresponding conditions. From SEM images in Figure S7, it can be concluded that the morphology of calcite on the acid treated surface is typically defective rhombohedral, which is quite different from those on the alkali treated surface and steel surface. This difference could be attributed to the effect of substrate surface groups as will be discussed further below.

#### 4. DISCUSSION

**4.1. Adsorption Mechanism of  $\text{CaCO}_3$  Particles on Hard Surfaces.** We have shown that the orientation of surface, horizontal versus vertical, give two kinds of deposition processes of  $\text{CaCO}_3$  on the surface. As shown in Figures 11a and c and 12a and c, rhombohedral calcite crystals with 10  $\mu\text{m}$  size dominate on the horizontal surface. The size and shape of these particles are almost the same as those in the bulk solution. This fact indicates that one type of adsorption occurs on the horizontal surface, i.e., indirect adhesion of crystals precipitated in the bulk solution, and this indirect adhesion dominates on the horizontal surface.<sup>37</sup> When the surface orientation is vertical and not directly exposed to sedimentation, tiny single crystals and amorphous particles (about 0.1 or 1  $\mu\text{m}$ ) dominate on the surface (Figures 11 b and d and 12b and d). The size and shape of these tiny crystals are quite different from those precipitated in the bulk solution, which suggests that these particles are

surface nucleated and grow by direct crystallization from lattice ions in the bulk solution. This direct growth on the surface is dominating on the vertical surface. From the images on the vertical surface (Figures 11b and d and 12b and d), we suggest that three stages of the initial growth process of calcite crystal occur. At the initial stage, the nanoparticles of amorphous  $\text{CaCO}_3$  initially formed on the steel surface, as shown in Figure 11b. The heights of the amorphous deposits were less than the width, i.e. the contact angles between the amorphous particle and the steel surface is very low.<sup>15</sup> Such a low contact angle is an indication that the amorphous particle almost completely wet the surface and heterogeneous nucleation of the amorphous particle may primarily occur for a high affinity on the surface. The second stage is the metastable stage (also shown in Figure 11b). At this stage, the amorphous  $\text{CaCO}_3$  have grown in the direction perpendicular to the steel surface and formed irregular rhombohedral calcite crystals (less than 1  $\mu\text{m}$ ). The appearance of these irregular calcite crystals suggests that this stage is an intermediate state between the amorphous and the stable regular crystal. Here the nonspherical  $\text{CaCO}_3$  could be regarded as the initial stage to form a cubic calcite crystal though these crystals are not yet fully developed. At the finally stable stage (Figure 11d), calcite crystals grow larger and complete, and their surface becomes smooth. It is likely that amorphous calcium carbonate was an intermediate state before the crystallization on the surface. However, the mechanism of transformation from the amorphous to the crystal state calls for further study.

**4.2. Formation of  $\text{CaCO}_3$  Deposits Depends on the Surface Properties.** The adsorbed amount of  $\text{CaCO}_3$  particle on the three kinds of surfaces (vertical surface) is significantly different judging from the ellipsometry results (Figures 4 and 5) even at the lower pH of 9.3 when precipitation in bulk solution is significantly lower as judged from the lower turbidity. Here we observed significant differences in the adsorbed amount depending on the surface properties where the adsorption decreases in the order stainless steel > acid treated silica > base treated silica. Similar trends are also observed on the SEM images recorded at the higher pH of 10, where bulk precipitation is significant. It is clear these effects can be attributed to the surface charge and the structure of the surfaces. Silicon surfaces always have an oxide layer that, when exposed to water, contains surface silanol groups. Silanol groups are amphoteric: they can act either as a donor or acceptor of a proton. The average charge density of the silica surface varies with the pH and added salt.<sup>38–40</sup> When the pH value of an aqueous solution is above pH 2.5, the net surface charge of silica is expected to be negative.<sup>39</sup> The difference of surface charge between acid treated silica surface and alkali treated silica surface is illustrated in Figure 13. The alkali treated silica surface has a relatively high negative surface charge in alkali solution, while the surface charge on the acid treated silica is lower. This has been verified with streaming potential data.<sup>46</sup> This might be related to the fact that the rehydration of silica is faster in alkaline solution.<sup>41</sup> The surface charge for stainless steel (304) is also pH dependent. The zero net charge (IEP) for stainless steel is attained at pH  $\sim$  3.4, resulting in a negative zeta potential for higher pH values.<sup>42</sup> We have previously discussed the importance of energetically favorable heterogeneous nucleation for the building up of the  $\text{CaCO}_3$  deposits, in particular on the vertical surfaces. Classical nucleation theory points out an importance of the interfacial energy for heterogeneous nucleation in supersaturated

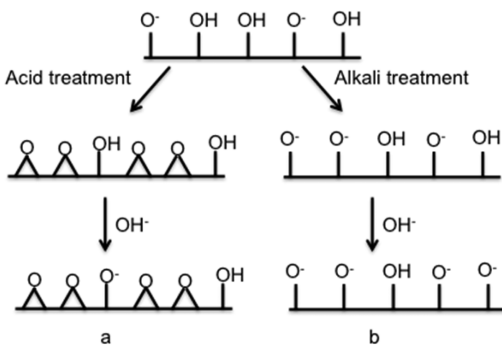


**Figure 13.** Schematic representation for silica surfaces in aqueous solution at pH 10: (a) acid treated silica surface; (b) alkali treated silica surface.

solutions including a substrate.<sup>43</sup> Ions adsorb on the surface as hydrated ions and the thickness of the adsorbed layer depend on their hydration enthalpies.<sup>44,45</sup> Therefore, it is reasonable to suppose that the presence of an interface has a large impact on the nucleation and the sequential crystal growth. If we for a moment neglect the effect of hydration, calcium ions are expected to have high affinity to the negatively charged silica surface in solution by electrostatic interaction between the ions and the surface, even before sodium carbonate has been added to the hard water. This adsorption of  $\text{Ca}^{2+}$  on the surface promotes the adsorption of  $\text{CO}_3^{2-}$  and can possibly also promote nucleation of  $\text{CaCO}_3$  particles. However, hydration and dehydration complicate this simplified view. It is beyond the scope of this study, but one can think that a more hydrated surface like the alkali treated silica surface, fewer hydrated ions are preferentially adsorbed in comparison with that of the acid treated silica surface. So the amount of particles on the alkali treated silica surface decreases sharply (Figure 4). However, when the surface orientation is horizontal, the deposition through sedimentation dominates on the surface and there is no significant difference in adsorbed amount on the two types of silica surface. For stainless steel surface, the interfacial behavior is closer to the acid treated silica surface. Furthermore, there are more nucleation sites on the steel surface because of the higher roughness. So the adsorbed amount of  $\text{CaCO}_3$  particle on stainless steel surface is larger than those on both types of silica surfaces. It can be concluded that conditions favorable for the adsorption and nucleation of calcium carbonate are determined by the electrostatic interaction between the hydrated calcium ion and the substrate as well as hydration effects.<sup>15</sup>

## 5. CONCLUSION

The kinetics of formation of  $\text{CaCO}_3$  precipitate in the bulk solution was studied by zeta potential, DLS, and turbidity measurements, while morphological and structural changes associated with the crystal growth in the bulk and on solid surfaces were studied with SEM and XRD. In-situ ellipsometry was used to follow the deposition kinetics on surfaces. The temperature has a major influence on the formation and growth of  $\text{CaCO}_3$  crystal both in the bulk solution and on hard surfaces. In the bulk solution, the rhombohedral calcite dominates and vaterite and amorphous  $\text{CaCO}_3$  transform to calcite with time at 25 °C, while at 55 °C aragonite dominates and the content of calcite increases with time. On hard surfaces, the rhombohedral calcite is dominant in all the samples and the adsorbed amount increases with time at 25 °C, whereas

distorted calcite and flowerlike aragonite dominate on the surface at 55 °C. It can be concluded the rhombohedral-shaped calcite more favorably adhere to solid surfaces than other types of crystals. Surface nucleation occurs on vertically placed silica and stainless steel surfaces, and when the surfaces are oriented horizontal, and thus exposed to sedimentation, particles formed in bulk solution seems to be dominating the deposited layer. The amount deposited on the vertical surfaces decreases in the order stainless steel surface > acid treated silica surface > alkali treated silica surface, and the adsorbed amount on horizontal surface is significantly larger than on the vertical surface. For the horizontal surface, the deposited amount is almost the same for all types of surfaces.

## ■ ASSOCIATED CONTENT

### Supporting Information

Figure S1 showing size distribution of the  $\text{CaCO}_3$  and SEM micrographs S2–S7 showing the kinetics of the deposition. This material is available free of charge via the Internet at <http://pubs.acs.org.org>.

## ■ AUTHOR INFORMATION

### Corresponding Author

\*E-mail: Tommy.Nylander@fkem1.lu.se. Phone: +46 46 222 8158. Fax: +46 46 222 4413.

### Notes

The authors declare no competing financial interest.

## ■ ACKNOWLEDGMENTS

This project was funded by BASF-SE, Ludwigshafen. T.N. and V.A. gratefully acknowledge support from the Swedish Research Council (VR) through the Linnaeus grant Organizing Molecular Matter (OMM) (239-2009-6794) and from Swedish Foundation for Strategic Research.

## ■ REFERENCES

- (1) Plummer, L. N.; Bunsenberg, E. *Cosmochim. Acta*. **1982**, *46*, 1011–1040.
- (2) Dickinson, S. R.; McGrath, K. M. *Cryst. Growth Des.* **2004**, *4*, 1411–1418.
- (3) Yamaguchi, T.; Murakava, K. *J. Soc. Mater Sci. (Japan)* **1981**, *30*, 856–860.
- (4) Taft, W. H. In *Developments in Sedimentology*; Chilingar, G. V., Bissell, H. J., Fairbridge, R. W., Eds.; Elsevier B.V.: Amsterdam, Holland, 1967; Vol. 9B, p 151.
- (5) Nancollas, G. H.; Sawada, K.; Shuttringer, E. In *Biomineralization and Biological Metal Accumulation*; Westbroek, P.; De Jong, E. W., Eds; Kluwer Academic Publishers Group: Dordrecht, Holland, 1983; p 155–169.
- (6) Yasue, T.; Mamiya, A.; Takahashi, Y.; Tsukisaka, R.; Arai, Y. *Nippon Kagaku Kaishi* **1984**, *7*, 1107–1113.
- (7) Sawada, K. *Pure Appl. Chem.* **1997**, *69*, 921–928.
- (8) Nancollas, G. H.; Reddy, M. N. *J. Colloid Interface Sci.* **1971**, *37*, 824–830.
- (9) Tai, Y. T.; Chen, F. B. *AIChE J.* **1998**, *44*, 1790–1798.
- (10) Hu, Z.; Deng, Y. *J. Colloid Interface Sci.* **2003**, *266*, 359–365.
- (11) Hu, Z.; Deng, Y. *Powder Technol.* **2004**, *140*, 10–16.
- (12) Spanos, N.; Koutsoukos, P. G. *J. Phys. Chem. B* **1998**, *102*, 6679–6684.
- (13) Wray, J. L.; Daniels, F. *J. Am. Chem. Soc.* **1957**, *79*, 2031–2034.
- (14) Takeshi, O.; Toshio, S.; Kiyoshi, S. *Geochim. Cosmochim. Acta* **1987**, *51*, 2757–2767.
- (15) Yamanaka, S.; Ito, N.; Shimosaka, A.; Shirakawa, Y.; Hidaka, J. *Cryst. Growth Des.* **2009**, *9*, 3245–3250.

- (16) Gabrielli, C.; Keddam, M.; Khalil, A.; Rosset, R.; Zidoune, M. *Electrochim. Acta* **1997**, *42*, 1207–1218.
- (17) Neville, A.; Hodgkiss, T.; Morizot, A. P. *J. Appl. Electrochem.* **1999**, *29*, 455–462.
- (18) Morizot, A.; Neville, A.; Hodgkiss, T. *J. Cryst. Growth.* **1999**, *198*, 738–743.
- (19) Neville, A.; Morizot, A. *Chem. Eng. Sci.* **2000**, *55*, 4737–4743.
- (20) Gabrielli, C.; Keddam, M.; Khalil, A.; Maurin, G.; Perrot, H.; Rosset, R.; Zidoune, M. *J. Electrochem. Soc.* **1998**, *145*, 2386–2396.
- (21) Gabrielli, C.; Keddam, M.; Perrot, H. *J. Appl. Electrochem.* **1996**, *26*, 1125–1132.
- (22) Gabrielli, C.; Maurin, G.; Poindessous, G.; Rosset, R. *J. Cryst. Growth* **1999**, *200*, 236–250.
- (23) Gracia, C.; Courbin, G.; Ropital, F.; Fiaud, C. *Electrochim. Acta* **2001**, *46*, 973–985.
- (24) Azzam, R. M. A.; Bashara, N. M. *Ellipsometry and Polarized Light*; North Holland: Amsterdam, 1989.
- (25) McCrackin, F. L.; Passaglia, E.; Stromberg, R. R.; Steinberg, H. *L. J. Res. Natl. Bur. Stand., Sect. A* **1963**, *67A*, 363–377.
- (26) Tiberg, F.; Landgren, M. *Langmuir* **1993**, *9*, 927–932.
- (27) Landgren, M.; Jönsson, B. *J. Phys. Chem.* **1993**, *97*, 1656–1660.
- (28) de Feijter, J. A.; Benjamins, J.; Veer, F. A. *Biopolymers* **1978**, *17*, 1759–1772.
- (29) Liu, J.; Pancera, S.; Boyko, V.; Gummel, J.; Nayuk, R.; Huber, K. *Langmuir* **2012**, *28*, 3593–3605.
- (30) Cuypers, P. A.; Corsel, J. W.; Janssen, M. P.; Kop, J. M. M.; Hermens, W. Th.; Hemke, H. C. *J. Biol. Chem.* **1983**, *258*, 2426–2431.
- (31) Ainalem, M.-L.; Campbell, R. A.; Nylander, T. *Langmuir* **2010**, *26*, 8625–8635.
- (32) Spanos, N.; Koutsoukos, P. G. *J. Cryst. Growth* **1998**, *191*, 783–790.
- (33) Zhang, Y.; Dawe, R. A. *Chem. Geol.* **2000**, *163*, 129–138.
- (34) Hartman, P. In *Crystal Growth: An Introduction*; Hartman, P., Ed.; North-Holland: Amsterdam, Holland, 1973; p 367.
- (35) Paquette, J.; Reeder, R. *J. Geochim. Cosmochim. Acta* **1995**, *59*, 735–749.
- (36) Wucher, B.; Yue, W.; Kulak, A. N.; Meldrum, F. C. *Chem. Mater.* **2007**, *19*, 1111–1119.
- (37) Abdel-Aal, N.; Satoh, K.; Sawada, K. *J. Cryst. Growth.* **2002**, *245*, 87–100.
- (38) Samoshina, Y.; Nylander, T.; Shubin, V.; Bauer, R.; Eskilsson, K. *Langmuir* **2005**, *21*, 5872–5881.
- (39) Bolt, G. H. *J. Phys. Chem.* **1957**, *61*, 1166–1169.
- (40) Nylander, T.; Samoshina, Y.; Lindman, B. *Adv. Colloid Interface Sci.* **2006**, *123–126*, 105–123.
- (41) Iler, R. K. *The chemistry of silica: solubility, polymerization, colloid and surface properties, and biochemistry*; Wiley: New York, NY, 1979.
- (42) Fernandes, C. M.; Senos, A. M. R.; Vieira, M. T. *Powder Technol.* **2006**, *164*, 124–129.
- (43) Mullin, J. W. *Crystallization*, 4th ed.; Butterworth-Heinemann: Oxford, U. K., 2001.
- (44) Higashitani, K.; Ishimura, K. *J. Chem. Eng. Jpn.* **1997**, *30*, 52–58.
- (45) Li, Y.; Kanda, Y.; Higashitani, K. *Adv. Powder Technol.* **2004**, *15*, 165–180.
- (46) Claesson, P. personal communication, Royal Institute of Technology, Stockholm, Sweden, 2012.